CrossMark

Enhanced electrochemical properties of MnO$_2$/PPy nanocomposites by miniemulsion polymerization

Fangnan Liang[1] · Zhiwei Liu[1] · Youzhi Liu[1]

Abstract In this study, manganese/polypyrrole (MnO$_2$/PPy) nanocomposites were facilely synthesized by an in situ miniemulsion polymerization method, and their morphologies and structures were characterized by transmission electron microscopy, Fourier transform infrared spectroscopy, X-ray diffraction and thermogravimetric analysis. The results showed that these MnO$_2$/PPy nanocomposites were quasi-spherical with a mean particle size of ~50 nm. The electrochemical performances were evaluated by cyclic voltammetry, electrochemical impedance spectroscopy, and galvanostatic charge-discharge measurements with a three-electrode cell system filled with 0.5 mol L^{-1} Na$_2$SO$_4$ solution. The results indicate that the specific capacitance of MnO$_2$/PPy nanocomposites was as high as 625 F g^{-1} at a current density of 0.5 A g^{-1} when the molar ratio of Py to KMnO$_4$ was 10:1. In addition, these MnO$_2$/PPy nanocomposites also show better long-term cycling stability and electrochemical reversibility than that prepared by traditional chemical methods. Thus, in situ miniemulsion polymerization can be a promising method for the preparation of MnO$_2$/PPy nanocomposites for supercapacitors, and MnO$_2$ and PPy can have a synergistic effect in improving the electrochemical properties of nanocomposites.

✉ Zhiwei Liu
  lzwww6723487@126.com

✉ Youzhi Liu
  lyzzhongxin@126.com

1   Shanxi Province Key Laboratory of Higee-Oriented
    Chemical Engineering, North University of China, No.
    3, Xueyuan Road, Jiancaoping District, Taiyuan 030051,
    People's Republic of China

1 Introduction

Pseudocapacitance supercapacitors are green power sources widely used in portable electronics, digital communication systems, power back-up systems, and hybrid electric vehicles [1–4]. As the specific capacitance, rate capability, and cycling stability of supercapacitors depend critically on the properties of electrode materials, numerous attempts have been made in recent years to develop efficient electrode materials [5]. Manganese oxide (MnO$_2$) is one of the most important pseudocapacitance materials with high theoretical capacitance (1370 F g^{-1}), low cost, environmental friendliness, and natural abundance. However, its application in supercapacitors can be limited due to its poor electrical conductivity [6]. Polypyrrole (PPy) is conductive polymer material with good electrical conductivity, unusual doping/dedoping process, environmental stability and flexible synthesis [7, 8], which can effectively improve the electrical conductivity of MnO$_2$. Recently, the MnO$_2$/PPy composites have attracted increasing research interest due to the synergistic effect of MnO$_2$ and PPy. As a result, the MnO$_2$/PPy composites could display excellent pseudocapacitive behavior in neutral electrolyte, thus making them attractive electrode materials for supercapacitors [9–11].

To the best of our knowledge, a variety of methods have been proposed for the synthesis of MnO$_2$/PPy nanocomposites, such as electrodeposition [12, 13], interfacial synthesis [14], self-assembly [15], and in situ chemical redox [16, 17]. Although the MnO$_2$/PPy thin film prepared by electrodeposition has a high performance, the loading amount of MnO$_2$ is extremely limited because over oxidation would destroy the π-conjugated structure of the polymers [18]. Li et al. prepared one-dimensional MnO$_2$/PPy nanorod composites adopting

methyl orange/FeCl$_3$ as the oxidant and self-degradable soft template, which had a specific capacitance of 328 F g^{-1} and good rate capability and cycling performance [19]. However, it is noted that these methods may have difficulties in producing a homogeneous polymerization environment on a molecular scale, and the synthesis process is complicated and uncontrollable. As a result, the final composites have a heterogeneous particle size distribution and prone to agglomeration, which can impact their electrochemical performances. Therefore, it is necessary to develop a controllable technology for the synthesis of the high-performance MnO$_2$/PPy nanocomposites.

Miniemulsion polymerization has emerged recently as a promising approach to prepare nanomaterials [20]. Miniemulsion facilities and emulsifier/stabilizer are two crucial factors for the preparation of miniemulsion. The commonly used miniemulsion facilities are sonicators and high pressure homogenizers [21]. Nanosized droplets (50–500 nm) can be generated by the mechanical effect resulting from the intense turbulence associated with shear and acoustic cavitation, and each droplet serves as an individual nanoreactor limiting the resulting particle size. The presence of emulsifier can delay the coalescence between droplets due to Brownian motion and Stokes law creaming. The stabilizer also builds up an Osmotic pressure in the droplets that can counteract the Laplace pressure, resulting in miniemulsion stability against Ostwald ripening [22]. As a result, the monomer droplets exist stably for a long time, and thus become the main place of polymerization. The obtained nanocomposites are superior to that prepared by chemical synthesis method, such as controlled growth of polymerization and a uniform droplet size distribution, and the miniemulsion synthesis process could be tailored to design new functional hybrid materials. Because of these advantages, miniemulsion polymerization has been successfully applied to the preparation of a series of hybrid nanomaterials, such as ZnO [23], PHEMA/CaCO$_3$ [24], SiO$_2$/Polystyrene [25], PCM/PPy [26], HAP [27], and magnetic nanoparticles [28]. However, to our knowledge, no MnO$_2$/PPy nanocomposites have been prepared by miniemulsion polymerization.

In this study, we synthesized MnO$_2$/PPy nanocomposites using miniemulsion as nanoreactors for a controlled and confined growth of nanoparticles. No expensive template, additional organic additives and complex precursors were involved in the synthesis pathway. The effect of the molar ratio of Py to KMnO$_4$ on the electrochemical performances of MnO$_2$/PPy nanocomposites was investigated. We showed that the enhanced electrochemical performances of as-prepared products were related to the synthesis technology and the synergistic effect of MnO$_2$ and PPy.

2 Experimental

2.1 Materials

Pyrrole (Py) monomer (Shanghai Macklin Biochemical Co., Shanghai, China), was distilled under reduced pressure and stored at a temperature below 4 °C until use. Potassium permanganate (KMnO$_4$), manganese sulfate hydrate (MnSO$_4$·H$_2$O), ferric chloride hexahydrate (FeCl$_3$·6H$_2$O), sodium dodecyl sulfate (SDS) surfactant, hexadecane (HD) stabilizer, cyclohexane (C$_6$H$_{12}$), and anhydrous ethanol were purchased from Tianjin Guangfu Fine Chemical Research Institute and used without further purification in this study. Distilled water was prepared using a GWA-UN to Pure & Ultrapure water purification system (Purkinje General).

2.2 Synthesis of MnO$_2$/PPy nanocomposites

MnO$_2$/PPy nanocomposites were prepared from Py and KMnO$_4$ by the in situ miniemulsion polymerization method. Firstly, 0.216 g of SDS was dissolved in 100 g of distilled water to prepare an aqueous phase, and 3 g of Py monomer and 0.75 g of HD were mixed with 15 g of CH to prepare an oil phase. The mixture was added dropwise to the aqueous phase under stirring for 20 min to produce a macroemulsion, followed by ultrasonication (Scientz-IID, 285 W, amplitude 30%) for 15 min under ice cooling to produce a miniemulsion. Secondly, a certain amount of KMnO$_4$ was dissolved in 50 g of distilled water, and then added dropwise into the above miniemulsion under magnetic stirring for 2 h. The molar ratio of Py to KMnO$_4$ was 5–20:1. Finally, the precipitates were centrifuged, washed with anhydrous ethanol and distilled water, and dried in a vacuum freeze dryer for 6 h to obtain MnO$_2$/PPy nanocomposites.

For comparison, pure MnO$_2$ was prepared by slowly adding KMnO$_4$ aqueous solution to 100 mL MnSO$_4$·H$_2$O solution and stirring for 6 h. The molar ratio of KMnO$_4$ to MnSO$_4$·H$_2$O was set to 2:3. Pure PPy was prepared as follows; typically, 3.78 g of FeCl$_3$·6H$_2$O was dissolved in 100 g of distilled water in a 250 mL three-necked flask. The mixture solution was stirred under N$_2$ protection for 20 min, and then 1 mL Py monomer (0.967 g) was rapidly added into the solution. The whole process was carried out in an ice bath. After 5 h of reaction, a dark product was separated from the solution by centrifugation, and then washed and dried as described previously.

2.3 Analysis and characterization

The bonding properties of MnO$_2$/PPy nanocomposites was characterized by Fourier transform infrared spectroscopy

(FTIR, Spectrum Two) using a standard potassium bromide (KBr) pellet technique. The crystalline structure was verified by X-ray diffraction (XRD, DX-2700) in the 2θ range of 10°–80° with a scanning speed of 5° min^{-1} and Cu K1 radiation. The morphology was determined by transmission electron microscopy (TEM, JEM-1400). The particle size distribution was determined by dynamic light scattering (DLS, Nano-ZS90). The thermogravimetric analysis was performed using a thermogravimetric analyzer (TGA, STA-449-F3) at 50–1000 °C at a heating rate of 10 °C min^{-1}.

2.4 Electrochemical measurements

All the electrochemical measurements were performed using a CHI 660E computer-controlled potentiostat. The three-electrode cell system was used to evaluate the electrochemical performances of the prepared electrode materials in 0.5 mol L^{-1} $NaSO_4$ aqueous electrolyte. The working electrodes were fabricated by mixing MnO_2/PPy nanocomposite powders, activated carbon and PVDF in a mass ratio of 7:2:1, which were then dispersed in an NMP solvent to form a homogeneous slurry. The slurry was coated onto a 1 cm^2 nickel foam and dried at 60 °C for 4 h to evaporate the solvent. Finally, the electrodes were pressed under 10 MPa for 10 min. The mass loading of the active materials was in the range of 1.5–2.0 mg cm^{-2}. A platinum wire electrode and a standard calomel electrode (SCE) were used as the counter electrode and the reference electrode, respectively. Cyclic voltammetry (CV) and galvanostatic charge-discharge measurements were conducted using the workstation. Electrochemical impedance spectroscopy (EIS) was conducted at open circuit potential over the frequency range 100 kHz to 10 mHz with a potential amplitude of 5 mV. All measurements were performed at room temperature. The specific capacitance of the electrodes was calculated from the discharging curves according to the following Eq. (1):

$$C = \frac{I \cdot \Delta t}{m \cdot \Delta V} \tag{1}$$

where C (F g^{-1}) is the specific capacitance, I (A) is the discharge current, Δt (s) is the discharge time, m (g) is the mass of active materials in the electrode, and ΔV (V) is the potential window.

3 Results and discussion

3.1 The synthesis mechanism of MnO_2/PPy nanocomposites

In this study, a controlled one-step in situ chemical redox method was used to synthesize MnO_2/PPy nanocomposites through miniemulsion polymerization, which was schematically illustrated in Fig. 1. The miniemulsion polymerization technique involved MnO_2/PPy interfacial synthesis, where emulsifier was dissolved in an aqueous phase while the monomer and stabilizer were dissolved in an organic phase. The miniemulsion with nanosized monomer droplets was generated by ultrasound, and the droplets remained stable throughout the reaction due to the use of emulsifier/stabilizer. Moreover, each droplet served as an individual nanoreactor, so that a maximum of interfacial areas was obtained for the polymerization reaction [29]. As the $KMnO_4$ aqueous solution was added dropwise into the prepared miniemulsion, the polymerization was initiated at the interface between the nanometer sized oil droplets and the water phase. Thus, Mn^{7+} was reduced to Mn^{4+}, and Py was oxidized to PPy simultaneously [1]. The reaction can be simplified as Eq. (2):

$$KMnO_4 + Py \rightarrow MnO_2 + PPy \tag{2}$$

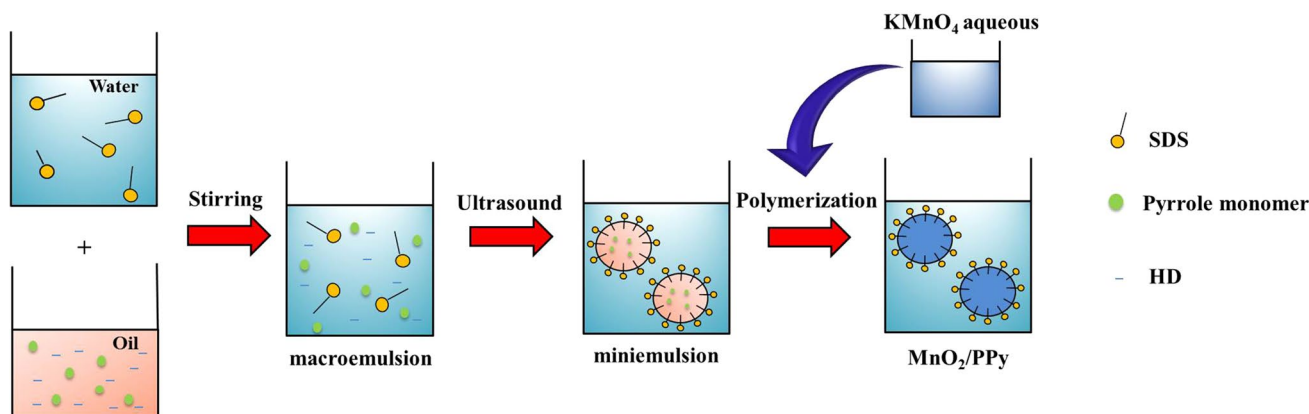The process of nuclei formation, growth, and aggregation were confined to the inorganic/organic interfacial

Fig. 1 A schematic illustration of the synthesis of MnO_2/PPy nanocomposites

regions, favoring the formation of quasi-spherical MnO_2/PPy nanocomposites with the mean particle size. During the miniemulsion process, ultrasound played an important role in the formation of uniform nanosized droplets. The shock waves and cavitation generated by ultrasound could disrupt particle aggregation and thus result in a better control of the mean size and size distribution. The unique droplet nucleation of miniemulsion would provide a new way to prepare polymers. We can also synthesize nanocomposites with different particle structures by appropriate handling of the interface effect [30].

3.2 Structure and morphology

The FTIR spectra of pure MnO_2, PPy and MnO_2/PPy nanocomposites are shown in Fig. 2. The peaks at approximately 3375 and 1624 cm^{-1} are normally attributed to the stretching vibration of –OH groups on the surface of the samples. For MnO_2, the peak at 563 cm^{-1} corresponds to the characteristic bending vibration of Mn–O bonds (curve a). Compared with MnO_2, several new peaks ascribed to PPy are observed in the FTIR spectra of MnO_2/PPy (curve b). The peaks at 1562 and 1374 cm^{-1} are attributed to the backbone stretching vibration of C=C and C–C in pyrrole ring. It is known that the skeletal vibrations involve the interactions of delocalized π-electrons [31]. The peak at 1343 cm^{-1} is due to =C–H in-plane deformation vibration, and that at 1303 cm^{-1} is due to C–N stretching vibration. The band at 1084 cm^{-1} is assigned to the N–H in-plane deformation vibration of the pyrrole ring, and a weak band at 958 cm^{-1} is assigned to the C–H out-of-plane stretching vibration absorption. All characteristic peaks of MnO_2 and PPy are observed (curve b), indicating that MnO_2/PPy nanocomposites have been successfully synthesized by the miniemulsion polymerization method.
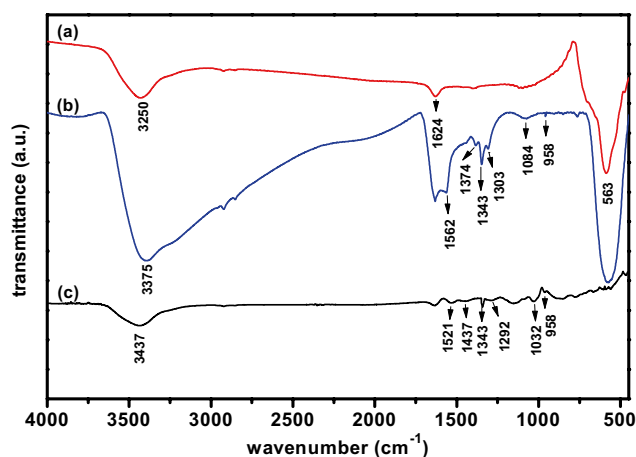
Figure 3 shows the XRD patterns of MnO_2, PPy and MnO_2/PPy nanocomposites. The sharp diffraction peaks of MnO_2 imply that MnO_2 is crystalline in nature (curve a). The diffraction peaks at 21.7°, 37.1°, 42.4°, 56.0° and 66.7° are assigned to the characteristic peaks of birnessite-type MnO_2 (Standard PDF Card), which correspond to the crystal planes of (002), (100), (101), (102) and (110), respectively. PPy nanoparticles exhibit a broad peak at 2θ values from 15° to 30°, suggesting the amorphous characteristic of PPy (curve b), which is consistent with the results reported by Li et al. [19] and Wang et al. [32]. According to curve c, it is clear that only three broad peaks of MnO_2 are present in MnO_2/PPy nanocomposites, and the broad peak from PPy with much less intensity is observed. This phenomenon could be attributed to the distortion of the crystal structure of MnO_2 particles into amorphous phase during the polymerization reaction [33].

Figure 4a shows the TEM image of MnO_2/PPy nanocomposites. Apparently, MnO_2/PPy nanocomposites are quasi-spherical with a uniform particle size distribution. The surface of these nanocomposites is rough, and the average particle size is about 50 nm. Figure 4b shows the distribution of the hydrodynamic size measured by DLS. It shows that the hydrodynamic size is much larger than that measured by TEM, probably due to the water molecules on the surface of nanocomposites and the hydrate water in the nanocomposites. The plot of particle size distribution could reflect the aggregation degree of as-prepared MnO_2/PPy nanocomposites. Figure 4b shows a narrow particle size distribution of MnO_2/PPy nanocomposites, which is consistent with the TEM results. Compared with traditional methods, the particle size distribution and dispersibility of nanocomposites prepared by miniemulsion polymerization are significantly improved.


Fig. 2 The FTIR spectra of *a* MnO_2, *b* MnO_2/PPy nanocomposites and *c* PPy
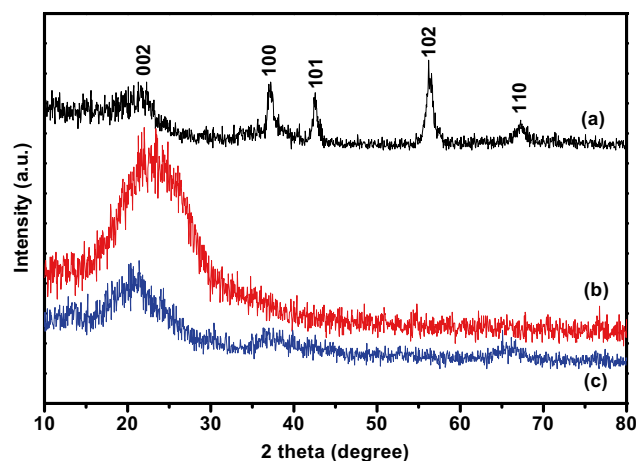
Fig. 3 The XRD patterns of *a* MnO_2, *b* PPy, and *c* MnO_2/PPy nanocomposites
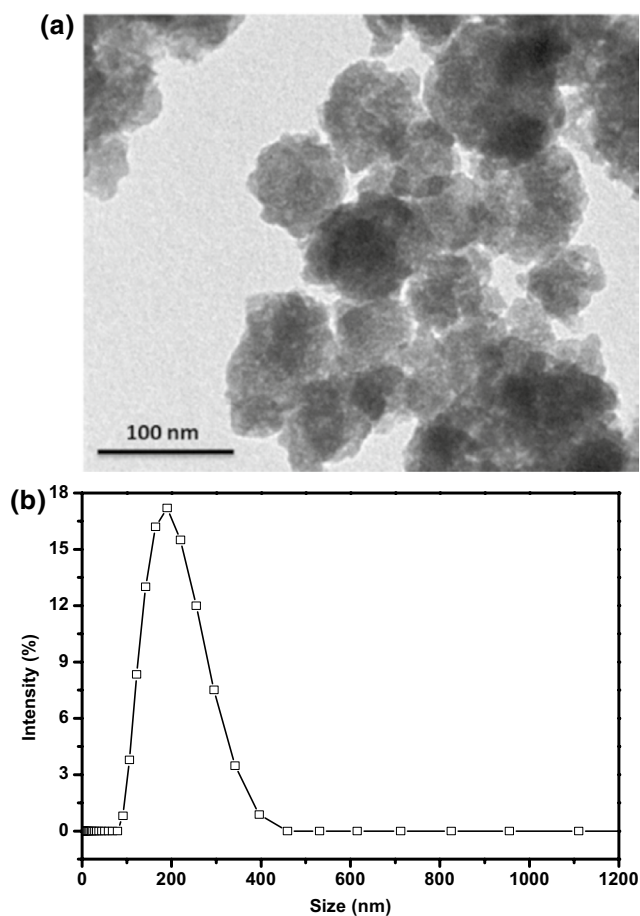
Fig. 4 a TEM image and **b** particle size distribution of MnO₂/PPy nanocomposites

Figure 5 shows the TGA curve of MnO₂/PPy nano-composites. Three weight-loss stages are observed in the TGA curve of MnO₂/PPy nanocomposites. In the first stage, a sharp decrease of 12.4% is observed from room
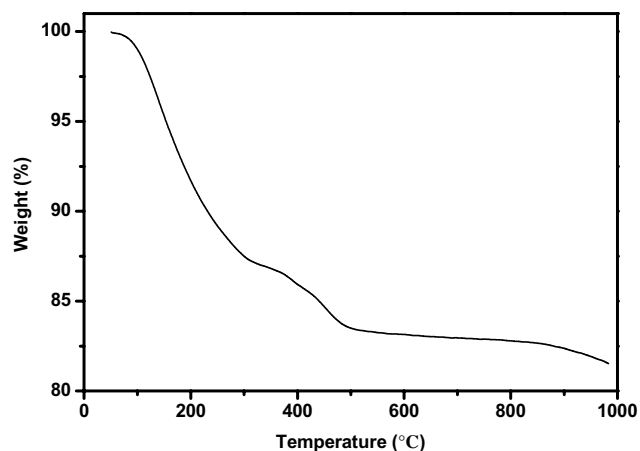
temperature to 300 °C, which is attributed to the loss of water and the adsorbed surfactants in the nanocomposites. The second weight loss stage occurs at 300–500 °C due to the decomposition of PPy skelecton. Accordingly, it implies that PPy is present in MnO₂/PPy nanocomposites with a mass content of ~4.2%. The third weight loss stage occurs at >600 °C due to the self-decomposition of MnO_2 to Mn_2O_3 [34]. A higher temperature would result in enhanced weight loss. The residual percentage of MnO_2/PPy is ~82%. The TGA results indicate that MnO_2/PPy nanocomposites have good thermal stability, probably due to the coordination bond interaction between MnO_2 and PPy chains described as before.

3.3 Electrochemical measurements

The electrochemical capacitive properties of MnO_2, PPy and MnO_2/PPy nanocomposites electrodes were investigated by CV and galvanostatic charge/discharge cycling in the three-electrode cell system. As shown in Fig. 6a,
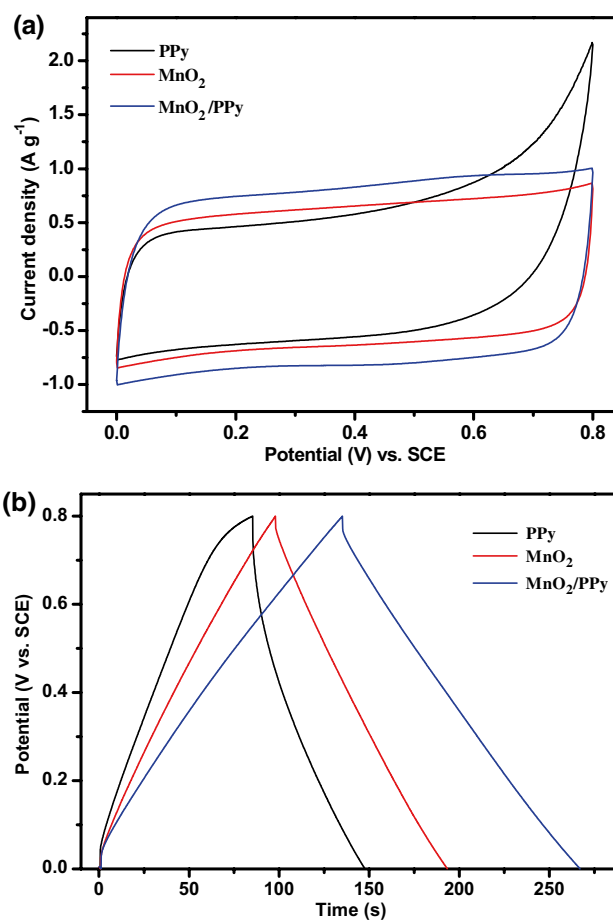
**Fig. 6** Electrochemical performances of MnO₂, PPy and MnO₂/PPy nanocomposites electrodes in 0.5 mol L⁻¹ Na₂SO₄: **a** CV curves at 5 mV s⁻¹ and **b** galvanostatic charge/discharge plots at 1 A g⁻¹

Fig. 5 The TGA curve of MnO₂/PPy nanocomposites

Fig. 7 Electrochemical performances of MnO_2/PPy nanocomposites ▶ electrodes in 0.5 mol L^{-1} Na_2SO_4: **a** CV curves for different molar ratios of Py to $KMnO_4$, **b** CV curves for different scan rates, **c** galvanostatic charge/discharge plots for different current densities, and **d** Nyquist plots of EIS. *Inset* is a magnified portion of the high-frequency region

MnO_2 and MnO_2/PPy nanocomposites electrodes exhibit quasi-rectangular and enantiomorphous features compared with PPy electrode. Typically, MnO_2/PPy nanocomposites electrode show a much larger current area than MnO_2 electrode. The galvanostatic charge/discharge curves of prepared electrodes at a current density of 1 A g^{-1} are displayed in Fig. 6b. Notably, the specific capacitance of MnO_2/PPy nanocomposites electrode (594 F g^{-1}) is much higher than that of MnO_2 and PPy electrodes (429 and 280 F g^{-1}), respectively. These results were in agreement with the CV results.

Figure 7a shows the CV curves of MnO_2/PPy electrodes with different molar ratios of Py to $KMnO_4$ at a scan rate of 5 mV s^{-1} in 0.5 mol L^{-1} Na_2SO_4 solution. All CV curves show a quasi-rectangular shape, indicating ideal pseudocapacitive behavior and fast reversible Faradic reactions of MnO_2/PPy nanocomposites. The current area increases with the increase of the molar ratio at first until the optimum molar ratio of 10:1 is reached, and then decreases with further increase of the molar ratio, indicating that the highest capacitance can be obtained at a molar ratio of 10:1. In addition, the CV curves also deviate from the rectangular shape at higher molar ratios. This is because a low content of $KMnO_4$ in the system can not completely oxidize the Py monomer. As a result, the structure of the nanocomposites is unstable, which can impact the synergistic effect of MnO_2 and PPy and also the electrochemical performances of nanocomposites.

Figure 7b shows the effect of scan rates on the electrochemical performances of MnO_2/PPy nanocomposites with the optimum molar ratio of 10:1. The curves gradually deviate from the quasi-rectangular shape with the increase of the scan rate. The rectangular shape is well maintained at a high scan rate of 50 mV s^{-1}, indicating good rate capability of the nanocomposite electrodes. Nevertheless, the rectangular shape is slightly distorted at 100 mV s^{-1}, due to the poor diffusion of electrolyte ions to the inner active regions of the electrode at high scan rates. Moreover, polarization resistance exists in the system [35]. Figure 7c displays the galvanostatic charge/discharge curves of nanocomposites at various current densities from 0.5 to 20 A g^{-1}. The typical triangular shape suggests superior reversibility of charging and discharging reactions of the electrode. The specific capacitance of the MnO_2/PPy electrode calculated from Eq. (1) are 625, 594, 540, 427, 284 and 90 F g^{-1} at a current density of 0.5, 1, 2, 5, 10
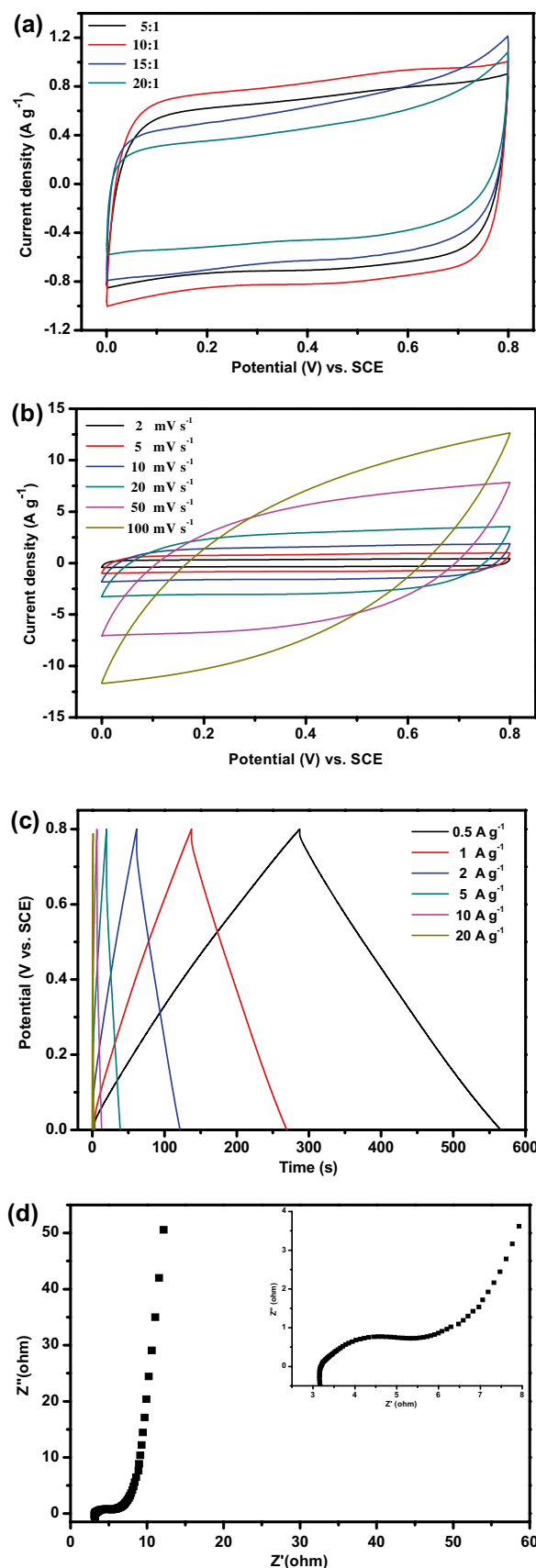
and 20 A g^{-1}, respectively. Thus, the nanosized composites are able to provide a larger specific surface area, which is conductive to improve the electrolyte accessibility and the effectively use of electrodes and thus result in a higher electrochemical performances.

EIS was performed to further demonstrate the electrochemical and structural properties of MnO_2/PPy nanocomposites with the optimum molar ratio of 10:1. As shown in Fig. 7d, the Nyquist plots have a small semicircle in the high frequency region and an inclined line in the low frequency region. The equivalent series resistance (R_s) could be extracted from the x-intercept, which is attributed to the resistance of the electrolyte, the contact resistance between the active material, electrolyte and current collector, and the intrinsic resistance of the active material. The semicircle diameter in the high frequency region corresponds to the charge transfer resistance (R_{ct}) which typically represents the resistance of electrochemical reactions on the electrode, namely, the Faraday resistance. The miniemulsion polymerization achieves the R_s/R_{ct} value of 3.2/2 Ω, which was lower than the traditional method of 4/2.9 Ω [5]. The lower resistance obtained in our study may be explained by the fact that miniemulsion polymerization can provide a more homogeneous polymerization environment and uniform particle size than the traditional methods. Apparently, the curves tend to a vertical line in the low frequency region, indicating that these nanocomposites display a nearly ideal capacitive behavior and good ions diffusion. These results demonstrate that MnO_2/PPy nanocomposites prepared by miniemulsion polymerization are particularly promising electrode materials for high-rate supercapacitors.

Long-term cycling life is an important requirement for supercapacitor electrodes. The cycling life test over 1000 cycles for optimized MnO_2/PPy electrode was evaluated by galvanostatic charge/discharge test at 1 A g^{-1}, and the results are shown in Fig. 8. The specific capacitance is decreased by ~3.4% in the first 100 cycles, but only 0.2% in the rest 900 cycles, indicating that MnO_2/PPy electrode has a good cycling life. The initial decrease of the specific capacitance may be attributed to the dissolution and/or detachment of unstable components in the electrolyte solution [36]. MnO_2/PPy electrodes have an excellent cycling stability with a high specific capacitance retention of 96.4% after 1000 cycles. The results imply that MnO_2/PPy nanocomposites exhibit significance cycling stability as an electrode for high-performance supercapacitors.

The high specific capacitance and the long-term cycling stability of MnO_2/PPy nanocomposites are attributed to the synergistic effect of MnO_2 and PPy. The MnO_2 in nanocomposites provide rigid support for the stability of the PPy chains during redox cycling [37], which in turn can enhance the conductivity of composites and prevent MnO_2 from dissolving in the electrolyte. Additionally, both
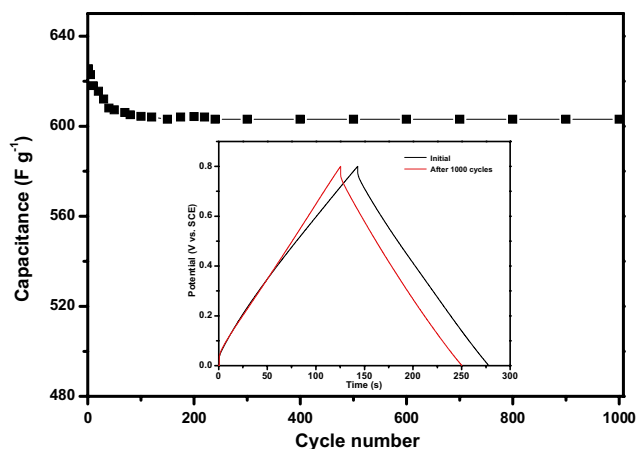
Fig. 8 Cycling stability of MnO_2/PPy nanocomposites electrode (10:1) at 1 A g^{-1} for 1000 cycles. The *inset* shows the charge-discharge curves for the 1st and 1000th cycles

MnO_2 and PPy have good pseudocapacitive behavior in the Na_2SO_4 neutral electrolyte. Thus, the cooperation ensures the structural integrity of MnO_2/PPy nanocomposites and thus the excellent electrochemical performances. Wang et al. [38] showed that the specific capacitance of coaxial MnO_2/PPy nanotubular composites was 337 F g^{-1} at a current density of 0.5 A g^{-1}. The nanocomposites prepared by miniemulsion polymerization showed a specific capacitance of about 625 F g^{-1} at the same current density. The capacitance retention of MnO_2/PPy nanocomposites was 96.5% after 400 cycles in a previous study [39], while it is 96.4% after 1000 cycles in this study. The electrode capacitance depends primarily on the properties of the materials. Miniemulsion polymerization enables the MnO_2/PPy nanocomposites to have a uniform particle size distribution and high surface area, which can greatly improve the electrochemical performances. Therefore, the miniemulsion polymerization technique is a promising method to prepare nanocomposites.

4 Conclusions

In summary, MnO_2/PPy nanocomposites with a quasispherical structure were successfully synthesized by miniemulsion polymerization for the first time. The effect of the molar ratio of Py to $KMnO_4$ and the electrochemical properties of MnO_2/PPy nanocomposites under optimum conditions were investigated. The results suggest that miniemulsion polymerization could effectively suppress the overgrowth of nuclei, leading to the formation of MnO_2/PPy nanocomposites with a diameter of <50 nm. The optimum molar ratio of Py to $KMnO_4$ was 10:1. The synergistic effect of MnO_2 and PPy enables MnO_2/PPy

nanocomposites electrode to have a higher specific capacitance than pure MnO_2 and PPy. In addition, these MnO_2/PPy nanocomposites have a high specific capacitance of 625 F g^{-1} at a current density of 0.5 A g^{-1}, and the specific capacitance retention was 96.4% after 1000 cycles. In short, miniemulsion polymerization provides an efficient and controllable approach for the preparation of MnO_2/PPy nanocomposites.

References

1. J.G. Wang, F.Y. Kang, B.Q. Wei, Prog. Mater. Sci. **74**, 51–124 (2015)
2. P.Y. Tang, L.J. Han, A. Genc, Y.M. He, X. Zhang, L. Zhang, J.R.G. Mascaros, J.R. Morante, J. Arbiol, Nano Energy **22**, 189–201 (2016)
3. J.S. Lee, D.H. Shin, J. Jang, Energy Environ. Sci. **8**, 3030–3039 (2015)
4. Y. Zhao, J. Misch, C.A. Wang, J. Mater. Sci. **27**, 5533–5542 (2016)
5. J.K. Gan, Y.S. Lim, N.M. Huang, H.N. Lim, Appl. Surf. Sci. **357**, 479–486 (2015)
6. G.Q. Han, Y. Liu, E. Kan, J. Tang, L.L. Zhang, H. H. Wang, W.H. Tang, RSC Adv. **4**, 9898–9904 (2014)
7. H. Farrokhi, O. Khani, F. Nemati, M. Jazirehpour, Synth. Met. **215**, 142–149 (2016)
8. L. Jiang, X. Lu, J. Xu, Y. Chen, G. Wan, Y. Ding, J. Mater. Sci. **26**, 747–754 (2015)
9. P. Li, Y. Yang, E. Shi, Q. Shen, Y. Shang, S. Wu, J. Wei, K. Wang, H. Zhu, Q. Yuan, A. Cao, D. Wu, Appl. Mater. Interfaces **6**, 5228–5234 (2014)
10. P.D. Oliveira, A. Helena, F. Nascimento, M. Luis, D. Oliveira, H. Pequeno, Mater. Res Ibero Am. J. **19**, 1080–1087 (2016)
11. J. Han, L.Y. Li, P. Fang, R. Guo, J. Phys. Chem. C **116**, 15900–15907 (2012)
12. S.N. Yang, P. Yan, Y.J. Li, K. Ye, K. Cheng, D.X. Cao, G.L. Wang, Q. Li, Electrochim. Acta **182**, 1153–1158 (2015)
13. L.J. Han, P.Y. Tang, L. Zhang, Nano Energy **7**, 42–51 (2014)
14. J.G. Wang, Y. Yang, Z.H. Huang, F.Y. Kang, J. Mater. Chem. **22**, 16943–16949 (2012)
15. H.Y. Zhou, Z. Yan, X. Yang, J. Lv, L.P. Kang, Z.H. Liu, Mater. Chem. Phys. **177**, 40–47 (2016)
16. O. Khani, F. Nemati, H. Farrokhi, M. Jazirehpour, Synth. Met. **220**, 567–572 (2016)
17. W. Yao, H. Zhou, Y. Lu, J. Power Sources **241**, 359–366 (2013)
18. W.Q. Ma, Q.Q. Shi, H.H. Nan, Q.Q. Hu, X.T. Zheng, B.Y. Geng, X.J. Zhang, RSC. Adv. **5**, 39864–39869 (2015)
19. J. Li, L. Cui, X.G. Zhang, Appl. Surf. Sci. **256**, 4339–4343 (2010)
20. J.M. Asua, Prog. Polym. Sci. **39**, 1797–1826 (2014)
21. J.M. Asua, Prog. Polym. Sci. **27**, 1283–1346 (2002)
22. K. Landfester, Angew. Chem. Int. Ed. **48**, 4488–4507 (2009)
23. M. Fricke, A. Voigt, P. Veit, K. Sundmacher, Ind. Eng. Chem. Res. **54**, 10293–10300 (2015)
24. Y. Fukui, K. Fujimoto, J. Mater. Chem. **22**, 3493–3499 (2012)
25. S.W. Zhang, S.X. Zhou, Y.M. Weng, L.M. Wu, Langmuir **21**, 2124–2128 (2005)
26. H.W. Ryn, S.P. Park, S.M. Lee, S.J. Lee, W.G. Koh, I.W. Cheong, J.H. Kim, Macromol. Res. **21**, 298–301 (2013)
27. A. Ethirajan, U. Ziener, K. Landfester, Chem. Mater. **21**, 2218–2225 (2009)
28. T. Staudt, T.O. Machado, N. Vogel, C.K. Weiss, P.H.H. Araujo, C. Sayer, K. Landfester, Macromol. Chem. Phys. **214**, 2213–2222 (2013)
29. S.S. Barkade, D.V. Pinjari, A.K. Singh, P.R. Gogate, J.B. Naik, S.H. Sonawane, M. Ashokkumar, A.B. Pandit, Ind. Eng. Chem. Res. **52**, 7704–7712 (2013)
30. M. Antonietti, K. Landfester, Prog. Polym. Sci. **27**, 689–757 (2002)
31. Y.L. Luo, L.H. Fan, F. Xu, Y.S. Chen, C.H. Zhang, Q.B. Wei, Mater. Chem. Phys. **120**, 590–597 (2010)
32. J.G. Wang, B.Q. Wei, F.Y. Kang, RSC Adv. **4**, 199–202 (2013)
33. J. Li, T.L. Que, J.B. Huang, Mater. Res. Bull. **48**, 747–751 (2013)
34. Y. Omomo, T. Sasaki, M. Watanabe, Solid State Ionics **151**, 243–250 (2002)
35. R.K. Sharma, A.C. Rastogi, S.B. Desu, Electrochim. Acta **53**, 7690–7695 (2008)
36. P. Soudan, J. Gaudet, D. Guay, D. Bélanger, R. Schulz, Chem. Mater. **14**, 1210–1215 (2002)
37. J. Joo, J.K. Lee, S.Y. Lee, K.S. Jang, E.J. Oh, A.J. Epstein, Macromolecules **33**, 5131–5136 (2000)
38. J.G. Wang, Y. Yang, Z.H. Huang, F.Y. Kang, Elctrochim. Acta **130**, 642–649 (2014)
39. L.Y. Yuan, C.Y. Wan, L.L. Zhao, Int. J. Electrochem. Sci. **10**, 9456–9465 (2015)